Spectral super-resolution reflectance retrieval from remotely sensed imaging spectrometer data

Jia, Guorui ; Hueni, Andreas ; Tao, Dongxing ; Geng, Ruonan ; Schaepman, Michael E ; Zhao, Huijie

Abstract: Existing atmospheric correction methods retrieve surface reflectance keeping the same nominal spectral response functions (SRFs) as that of the airborne/spaceborne imaging spectrometer radiance data. Since the SRFs vary dependent on sensor type and configuration, the retrieved reflectance of the same ground object varies from sensor to sensor as well. This imposes evident limitations on data validation efforts between sensors at surface reflectance level. We propose a method to retrieve super-resolution reflectance at the surface, by combining the first-principles atmospheric correction method FLAASH (fast line-of-sight atmospheric analysis of spectral hypercubes) with spectral super-resolution of imaging spectrometer radiance data. This approach is validated by comparing airborne AVIRIS (airborne visible/infrared imaging spectrometer) and spaceborne Hyperion data. The results demonstrate that the super-resolution reflectance in spectral bands with sufficiently high signal-to-noise ratio (SNR) serves as intermediate quantity to cross validate data originating from different imaging spectrometers.

DOI: https://doi.org/10.1364/OE.24.019905

Research Article | Vol. 24, No. 17 | 22 Aug 2016 | OPTICS EXPRESS 19905

Optics EXPRESS

Spectral super-resolution reflectance retrieval from remotely sensed imaging spectrometer data

GUORUI JIA,[1,2,4] ANDREAS HUENI,[2] DONGXING TAO,[1,3] RUONAN GENG,[1] MICHAEL E. SCHAEPMAN,[2] AND HUIJIE ZHAO[1,5]

[1]*School of Instrument Science & Opto-electronics Engineering, Beihang University, Beijing, 100191, China*
[2]*Remote Sensing Laboratories, University of Zurich, CH-8057 Zurich, Switzerland*
[3]*Currently with Beijing Institute of Spacecraft Environment Engineering, Beijing, 100094, China*
[4]*jiaguorui@buaa.edu.cn*
[5]*hjzhao@buaa.edu.cn*

Abstract: Existing atmospheric correction methods retrieve surface reflectance keeping the same nominal spectral response functions (SRFs) as that of the airborne/spaceborne imaging spectrometer radiance data. Since the SRFs vary dependent on sensor type and configuration, the retrieved reflectance of the same ground object varies from sensor to sensor as well. This imposes evident limitations on data validation efforts between sensors at surface reflectance level. We propose a method to retrieve super-resolution reflectance at the surface, by combining the first-principles atmospheric correction method FLAASH (fast line-of-sight atmospheric analysis of spectral hypercubes) with spectral super-resolution of imaging spectrometer radiance data. This approach is validated by comparing airborne AVIRIS (airborne visible/infrared imaging spectrometer) and spaceborne Hyperion data. The results demonstrate that the super-resolution reflectance in spectral bands with sufficiently high signal-to-noise ratio (SNR) serves as intermediate quantity to cross validate data originating from different imaging spectrometers.

OCIS codes: (100.1830) Deconvolution; (100.3190) Inverse problems; (100.6640) Superresolution; (110.4234) Multispectral and hyperspectral imaging; (300.6490) Spectroscopy, surface.

References and links

1. G. Schaepman-Strub, M. E. Schaepman, T. H. Painter, S. Dangel, and J. V. Martonchik, "Reflectance quantities in optical remote sensing—definitions and case studies," Remote Sens. Environ. **103**(1), 27–42 (2006).
2. B.-C. Gao, K. B. Heidebrecht, and A. F. H. Goetz, "Derivation of scaled surface reflectance from AVIRIS data," Remote Sens. Environ. **44**(2-3), 165–178 (1993).
3. M. W. Matthew, S. M. Adler-Golden, A. Berk, S. C. Richtsmeier, R. Y. Levine, L. S. Bernstein, P. K. Acharya, G. P. Anderson, G. W. Felde, M. P. Hoke, A. Ratkowski, H. Burke, R. D. Kaiser, and D. P. Miller, "Status of atmospheric correction using a MODTRAN4-based algorithm," Proc. SPIE **4049**, 199–207 (2000).
4. T. Perkins, S. Adler-Golden, M. W. Matthew, A. Berk, L. S. Bernstein, J. Lee, and M. Fox, "Speed and accuracy improvements in FLAASH atmospheric correction of hyperspectral imagery," Opt. Eng. **51**(11), 111707 (2012).
5. C. J. Miller, "Performance assessment of ACORN atmospheric correction algorithm," Proc. SPIE **4725**, 438–449 (2002).
6. R. Richter and D. Schläpfer, "Geo-atmospheric processing of airborne imaging spectrometry data. Part 2: atmospheric/topographic correction," Int. J. Remote Sens. **23**(13), 2631–2649 (2002).
7. Z. Qu, B. C. Kindel, and A. F. H. Goetz, "The high accuracy atmospheric correction for hyperspectral data (HATCH) model," IEEE Trans. Geosci. Remote Sens. **41**(6), 1223–1231 (2003).
8. R. Richter, "Bandpass-resampling effects on the retrieval of radiance and surface reflectance," Appl. Opt. **39**(27), 5001–5005 (2000).
9. R. N. Clark, T. V. V. King, M. Klejwa, G. Swayze, and N. Vergo, "High spectral resolution reflectance spectroscopy of minerals," J. Geophys. Res. **95**(B8), 12653–12680 (1990).
10. F. A. Kruse, "The effects of spatial resolution, spectral resolution, and SNR on geologic mapping using hyperspectral data, northern Grapevine Mountains, Nevada," in *Proceedings of the 9th JPL Airborne Earth Science Workshop* (JPL Publication, 2000), pp. 261–269.

#267454 http://dx.doi.org/10.1364/OE.24.019905
Journal © 2016 Received 16 Jun 2016; revised 12 Aug 2016; accepted 13 Aug 2016; published 19 Aug 2016

Optics EXPRESS

11. G. A. Swayze, R. N. Clark, A. F. H. Goetz, T. G. Chrien, and N. S. Gorelick, "Effects of spectrometer band pass, sampling, and signal-to-noise ratio on spectral identification using the Tetracorder algorithm," J. Geophys. Res. **108**(E9), 5105 (2003).
12. P. D'Odorico, A. Gonsamo, A. Damm, and M. E. Schaepman, "Experimental evaluation of Sentinel-2 spectral response functions for NDVI time-series continuity," IEEE Trans. Geosci. Remote Sens. **51**(3), 1336–1348 (2013).
13. *ASD Technical Guide,* 3rd ed. (Analytical Spectral Devices, Inc., 1999).
14. T. Dongxing, Z. Huijie, J. Guorui, and Y. Yan, "Analyzing the effect of synthetic scene resolution, sampling interval, and signal-to-noise ratio on hyperspectral imaging sensor simulations," Appl. Opt. **53**(28), 6375–6381 (2014).
15. H. Zhao, G. Jia, and N. Li, "Transformation from hyperspectral radiance data to data of other sensors based on spectral superresolution," IEEE Trans. Geosci. Remote Sens. **48**(11), 3903–3912 (2010).
16. G. P. Anderson, A. Berk, P. K. Acharya, M. W. Matthew, L. S. Bernstein, J. H. Chetwynd, Jr., H. Dothe, S. M. Adler-Golden, A. J. Ratkowski, G. W. Felde, J. A. Gardner, M. L. Hoke, S. C. Richtsmeier, B. Pukall, J. B. Mello, and L. S. Jeong, "MODTRAN4: radiative transfer modeling for remote sensing," Proc. SPIE **3866**, 2–10 (1999).
17. M. K. Griffin, H. K. Burke, D. Mandl, and J. Miller, "Cloud cover detection algorithm for EO-1 Hyperion imagery," Proc. SPIE **5093**, 483–494 (2003).
18. B.-C. Gao, Y. J. Kaufman, D. Tanré, and R.-R. Li, "Distinguishing tropospheric aerosols from thin cirrus clouds for improved aerosol retrievals using the ratio of 1.38-μm and 1.24-μm channels," Geophys. Res. Lett. **29**(18), 1890 (2002).
19. Y. J. Kaufman, A. E. Wald, L. A. Remer, B.-C. Gao, R.-R. Li, and L. Flynn, "The MODIS 2.1-μm channel–correlation with visible reflectance for use in remote sensing of aerosol," IEEE Trans. Geosci. Remote Sens. **35**(5), 1286–1298 (1997).
20. F. A. Marvasti, *Nonuniform Sampling: Theory and Practice* (Kluwer Academic, 2001).
21. G. Jia, H. Zhao, and N. Li, "Simulation of hyperspectral scene with full adjacency effect," in *Proceedings of 2008 IEEE International Geoscience and Remote Sensing Symposium* (IGARSS 2008), pp. III-724.
22. R. O. Green, M. L. Eastwood, C. M. Sarture, T. G. Chrien, M. Aronsson, B. J. Chippendale, J. A. Faust, B. E. Pavri, C. J. Chovit, M. Solis, M. R. Olah, and O. Williams, "Imaging spectroscopy and the Airborne Visible/Infrared Imaging Spectrometer (AVIRIS)," Remote Sens. Environ. **65**(3), 227–248 (1998).
23. R. N. Clark and G. A. Swayze, "Evolution in imaging spectroscopy analysis and sensor signal-to-noise: an examination of how far we have come," in *Proceedings of the 6th JPL Airborne Earth Science Workshop* (1996), pp. 49–53.
24. J. S. Pearlman, P. S. Barry, C. C. Segal, J. Shepanski, D. Beiso, and S. L. Carman, "Hyperion: a space-based imaging spectrometer," IEEE Trans. Geosci. Remote Sens. **41**(6), 1160–1173 (2003).
25. E. Christophe, D. Leger, and C. Mailhes, "Quality criteria benchmark for hyperspectral imagery," IEEE Trans. Geosci. Remote Sens. **43**(9), 2103–2114 (2005).
26. C.-I. Chang, "An information-theoretic approach to spectral variability, similarity, and discrimination for hyperspectral image analysis," IEEE Trans. Inf. Theory **46**(5), 1927–1932 (2000).
27. R. Richter, D. Schläpfer, and A. Müller, "Operational atmospheric correction for imaging spectrometers accounting for the smile effect," IEEE Trans. Geosci. Remote Sens. **49**(5), 1772–1780 (2011).

1. Introduction

Remotely sensed imaging spectrometer data, also called hyperspectral images in remote sensing community, need to be corrected for the effects of illumination and atmosphere to retrieve surface hemispherical-conical reflectance factor (HCRF) [1], which is most often referred to as reflectance and is the usual starting point for application analysis. There are a few commercial atmospheric correction codes widely used to retrieve surface reflectance, including ATREM (Atmospheric REMoval program) [2], FLAASH (Fast Line-of-sight Atmospheric Analysis of Spectral Hypercubes) [3,4], ACORN (Atmospheric CORrection Now) [5], ATCOR (Atmospheric/Topographic Correction) [6], and HATCH (High-accuracy Atmospheric Correction for Hyperspectral Data) [7]. They all generate surface reflectance with the same number of spectral bands as the input radiance images which are bandpass sampling, also called convolution, of the actual at-sensor radiance with the spectral response functions (SRFs) of the corresponding imaging spectrometer [8].

However, the SRFs are determined by a set of parameters including center wavelength, full width at half maximum (FWHM), and bandpass shape. These parameters vary with differing imaging spectrometers. This results in discrepancies between the retrieved surface reflectance originating from different sensors [9–12]. In this circumstance, different feature positions, depths, and shapes of ground objects would be extracted. This presents a technical

Optics EXPRESS

barrier for cross-validation of reflectance data from different sensors and for the retrieval of stable spectral fingerprints.

In practice, interpolation [13] or convolution [11] methods are often used to unify the center wavelengths of data sets originating from different sensors for comparison. However, the FWHM (which is the index of spectral resolution) difference between sensors is ignored in the interpolation methods. In the convolution methods, the FWHM of the data being convolved is ignored and the full SRFs of the destination sensor are adopted as the convolution functions. This generates results with larger FWHM than the actual ones [14].

In the past, we have proposed a spectral super-resolution method for hyperspectral radiance data to suppress the FWHM and hence to support data simulation and cross calibration [15]. Through spectral super-resolution, radiance spectra with nominal zero FWHMs and arbitrary spectral sampling intervals (SSIs) can be retrieved. They retain much finer spectral atmospheric absorption features, as shown in Fig. 1. Based on them, SRF transformation to simulate radiance data from other sensors for cross-calibration can be fulfilled more accurately.

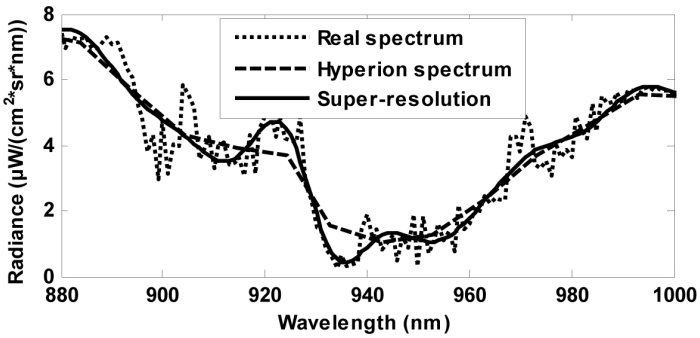

Fig. 1. Illustration of the effect of spectral super-resolution around the water vapor absorption feature at 940 nm. Taking MODTRAN4-simulated 1-nm spectral resolution top of atmosphere radiance as the real spectrum, simulated Hyperion spectrum was generated by convolution of it, and super-resolution spectrum was retrieved from the simulated Hyperion spectrum. Adopted from [15].

In this paper, we take a step forward by making improvements to the FLAASH method and retrieving super-resolution reflectance from the super-resolved radiance. The retrieved reflectance bears narrower FWHMs than the original radiance data, and this would support multi-source reflectance data comparison.

The rest of the paper is organized as follows. The scheme of and improvements to the FLAASH method is described in Section 2. The preliminary results about super-resolution reflectance retrieval and comparison based on AVIRIS (Airborne Visible/Infrared Imaging Spectrometer) and Hyperion images are illustrated in Section 3. In Section 4, the key factors affecting the results are discussed before we draw the conclusions.

2. Method

2.1 FLAASH atmospheric correction method

FLAASH solves the surface reflectance from at-sensor radiance in the solar-reflective spectral range through two steps [3,4]. The first is the retrieval of atmospheric status including cloud, aerosol, and water vapor information. The second is the solution of the core radiative transfer (RT) equation as

$$L = \frac{A\rho}{1-\rho_e S} + \frac{B\rho_e}{1-\rho_e S} + L_a, \tag{1}$$

Optics EXPRESS

based on the retrieved atmospheric parameters, where L is the at-sensor radiance, ρ the ground reflectance of the target, ρ_e the average reflectance of a large-scale background, A and B the effective coefficients dependent on illumination and atmospheric status, S the spherical albedo of the atmosphere, and L_a the path radiance. All of these variables depend on the spectral band, and the wavelength index has been omitted for simplicity. In this process, the RT code MODTRAN [16] is adopted to set up look-up tables (LUTs) for calculation of the coefficients in Eq. (1).

Several improvements to this process are proposed later on to make it compatible with the spectral super-resolution.

2.2 Cloud detection, visibility and column water vapor retrieval

The low-/mid-altitude cloud mask generation methods used in FLAASH [3] and in the EO-1 Extended Mission [17] are combined to detect opaque clouds in hyperspectral images. The adopted apparent-reflectance-based tests include 1) the brightness tests as $\rho_{660nm}>0.28$ and $\rho_{1255nm}>0.3$, 2) the color balance tests as $\rho_{660nm}/\rho_{860nm}\geq 0.5$, desert sand index (DSI)>0 and normalized difference snow index (NDSI)<0.4, and 3) the low water vapor test as (column water vapor)/average(column water vapor) $_{noncloud}<0.8$. The pixels that passed all the above tests are flagged as cloud pixels. The cloud mask generated through the above process is used to mask out the inappropriate pixels in the following visibility and column water vapor retrieval processes and to indicate the pixels with unreliable reflectance values in the final result.

Cirrus, i.e. high-altitude cloud, pixels are picked out according to a few other tests improved from [17,18]. They include 1) $\rho_{1375nm}>T_1$, 2) $0.9<\rho_{660nm}/\rho_{860nm}<1.1$, 3) $\rho_{1375nm}/\rho_{1640nm}>T_2$, and 4) $\rho_{1375nm}/\rho_{1240nm}>T_3$, in which thresholds T_1, T_2, and T_3 could be determined as the density slice position of the bimodal histogram composed of corresponding test values of all the pixels. A pixel is counted into the cirrus mask only if it passes all these tests. The cirrus mask is used in the same way as low-/mid-altitude cloud mask.

Visibility is defined in MODTRAN as surface meteorological range and related to aerosol extinction at 550 nm. Retrieval of it is based on the dark pixel method [19]. Approximate surface reflectance values of dark pixels at 660 nm and 2100 nm are determined based on MODTRAN calculations that use atmosphere model, aerosol model, and a series of visibility settings equally spaced in terms of aerosol optical depth. Then a LUT is set up between the visibility settings and the average values of the quantity $\rho_{660nm}-0.45*\rho_{2100nm}$ over all the dark pixels. An optimization generates the average visibility of the whole image by aiming at a zero average value of the above quantity based on the LUT.

Pixel-wise column water vapor retrieval is based on MODTRAN-generated LUT as well. In a spectral region covering one of the 1135 nm, 940 nm, and 820 nm water vapor absorption features, MODTRAN is run for a series of surface reflectance and atmospheric water vapor amounts. The MODTRAN-output radiance values at the absorption band and at related shoulder bands are selected to construct two 2-Dimensional (2-D) LUTs. The shoulder bands are the first bands, searching toward a shorter (left) and a longer (right) wavelength, just outside the absorption feature. In each of the 2-D LUTs, one dimension is the reflectance-dependent shoulder band value (either the left or the right one), while the other is the ratio between the shoulder and the absorption band values. The two LUTs are respectively used to determine two column water vapor amounts for each pixel and the average is taken as the retrieved amount.

2.3 Spectral super-resolution of radiance

For super-resolution reflectance retrieval, the cloud masks, visibility and column water vapor information are still retrieved from the hyperspectral images of original spectral resolution. But the input radiance to Eq. (1) should be super-resolved.

Optics EXPRESS

The super-resolution radiance $L(\lambda)$ can be restored by iterative de-correlating the SRFs from the spline interpolation of the N-band hyperspectral radiance $\overline{\boldsymbol{L}}$ as follows [15]:

$$L^0(\lambda) = spline\_interp(\overline{\boldsymbol{L}}^0) = spline\_interp(\overline{\boldsymbol{L}}), \tag{2}$$

$$\overline{L}_i^{'k} = \int L^k(\lambda)\cdot g_i(\lambda)\cdot d\lambda \Big/ \int g_i(\lambda)d\lambda \qquad i = 1,\cdots,N, \tag{3}$$

$$\overline{\boldsymbol{L}}^{'k} = \{\overline{L}_i^{'k} \mid i = 1,\cdots,N\}, \tag{4}$$

$$\overline{\boldsymbol{L}}^{k+1} = \overline{\boldsymbol{L}}^k + a\cdot(\overline{\boldsymbol{L}} - \overline{\boldsymbol{L}}^{'k}), \tag{5}$$

$$L^{k+1}(\lambda) = spline\_interp(\overline{\mathbf{L}}^{k+1}), \tag{6}$$

where $L^k(\lambda)$ is the k_{th} estimate of the super-resolution radiance with the initial value $L^0(\lambda)$, $\overline{\boldsymbol{L}}^k$ the k_{th} estimate of a discrete sampling of the super-resolution radiance, $\overline{\boldsymbol{L}}^0$ the initial value of $\overline{\boldsymbol{L}}^k$, $\overline{\boldsymbol{L}}^{'k}$ the bandpass sampling vector of the super-resolution radiance, $g_i(\lambda)$ the i_{th} band SRF, and a relaxation factor to accelerate the process. The iteration stops when the spectrum $\overline{\boldsymbol{L}}^{'k}$ approximates the observed spectrum $\overline{\boldsymbol{L}}$ well enough.

Obviously, the super-resolution radiance is an estimate of the actual continuous at-sensor radiance. From the signal theoretic perspective, the observed spectrum is the result of the following process. The actual continuous radiance spectrum is low-pass filtered and then non-uniformly sampled. The filters are the Gaussian SRFs that are shift-variant in the spectral dimension. In addition, the continuous signal can be recovered through an iterative method according to the non-uniform sampling theory [20]. The recovered signal bears no filtering effect. Actually, the super-resolution method exactly is this iterative recovery method. The super-resolution spectrum is hence a finite energy signal, with no bandpass sampling effects. In other words, the spectral resolution is extremely high in theory. Furthermore, it could be rendered at any SSI.

2.4 Super-resolution reflectance retrieval

Taking the super-resolution radiance as input in the reflectance retrieval process, super-resolution illumination and atmospheric coefficients, i.e. $A(\lambda)$, $B(\lambda)$, $S(\lambda)$ and $L_a(\lambda)$ in Eq. (1), should be calculated. To achieve this objective, the filter function in MODTRAN is set at its highest achievable spectral resolution as rectangle and exactly no overlap between adjacent bands. For example, both FWHM and SSI were set as fine as 1 nm throughout the solar-reflective spectral region (400 nm - 2500 nm), as we used MODTRAN4 that is based on a 1 cm^{-1} band model with triangular slit function. They could be set as 0.1 nm if it would be possible to use MODTRAN5 that is based on a 0.1 cm^{-1} band model. In this way, the coefficients extracted from the LUTs as a result of several MODTRAN simulations [21] are of the corresponding high spectral resolution, i.e. 1 nm currently due to MODTRAN4.

Correspondingly, the super-resolution radiance is spectrally resampled with this filter function to match the spectral resolution. Then it is low-pass filtered in the spatial dimension with a Gaussian filter related to the atmospheric adjacency effect to solve the average radiance L_e and consequently the average surrounding reflectance ρ_e:

$$L_e = \frac{(A+B)\rho_e}{1-\rho_e S} + L_a. \tag{7}$$

Optics EXPRESS

As a result, ρ_e keeps the same bandpass sampling effect as the atmospheric coefficients.

With all of these parameters, the surface reflectance of spectral super-resolution is determined finally according to Eq. (1).

3. Results

3.1 Atmospheric correction of AVIRIS data

The airborne AVIRIS [22] image was acquired on Jun. 19, 1997 over Cuprite mineral area, USA. AVIRIS comprises four spectrometer and detector assemblies to sample the 370 nm - 2507 nm spectra. The 5 overlapping bands (band 31, 32, 97, 98, 160) in the overlapping region of each two adjacent assemblies were discarded, and the remaining 219 bands make up the radiance image to be atmospherically corrected. The spectral resolution is about 10 nm and spatial resolution about 20 m.

The super-resolution reflectance image was retrieved under the parameter settings listed in Table 1. In the process, FWHM and SSI were both set as 1 nm to make full use of the spectral resolution of MODTRAN4.

Table 1. Settings in the reflectance retrieval.

Parameter	Value
Scene Center Latitude (°)	37.54 N
Scene Center Longitude (°)	117.21 W
Ground Elevation (km)	1.542
Sensor Altitude (km)	21.046
Flight Time (GMT)	19:47:48
Viewing Zenith Angle (°)	180
Atmospheric Model	Mid-latitude Summer
Aerosol Model	Rural
Visibility (km)	23
CO_2 Mixing Ratio (ppmv)	390
Water Vapor Retrieval Feature (nm)	1135
Aerosol Retrieval	None

Besides the super-resolution reflectance, the reflectance of the original spectral resolution was retrieved using FLAASH without spectral polishing and wavelength recalibration (to comply with the non-polishing and non-recalibration status of the super-resolution method). The parameter settings for FLAASH were the same as those in Table 1. In addition, the super-resolution reflectance data was convolved with the AVIRIS SRFs to generate reflectance with the same spectral sampling characteristics as the AVIRIS FLAASH reflectance. This AVIRIS-resolution reflectance derived from the super-resolution one can be directly compared with the AVIRIS FLAASH reflectance.

According to the Cuprite mineral map generated by Clark and Swayze based on AVIRIS 1995 data [23], four regions of interests (ROIs) were drawn to pick out pixels corresponding to Na-Montmorillonite, Kaolinite, K-Alunite, and Muscovite respectively, as shown in Fig. 2. The average spectra of each ROI from the above three results are plotted in Fig. 3.

It shows that the super-resolution reflectance keeps much more narrow spikes than the other relatively low resolution spectra, while the general shapes of them are similar. A strong similarity is also expressed by the convolved spectra with reference to the corresponding FLAASH spectra, except for the spectral regions around 760 nm, 940 nm, 1100 nm - 1150 nm and beyond 2300 nm. These exceptional regions associate with the strong absorption features of oxygen and water vapor in the atmosphere respectively, where AVIRIS holds low signal-to-noise ratio (SNR, cf. figure 9 in [22]). The regions 1330 nm - 1430 nm and 1800 nm - 1950 nm should be ignored because there is little information about ground objects as a result of the severe absorption by water vapor along the RT path and these bands are set as bad bands in the FLAASH results. The relative deviation is generally lower than ± 5% for the high-SNR bands, as shown in Fig. 4.

Optics EXPRESS

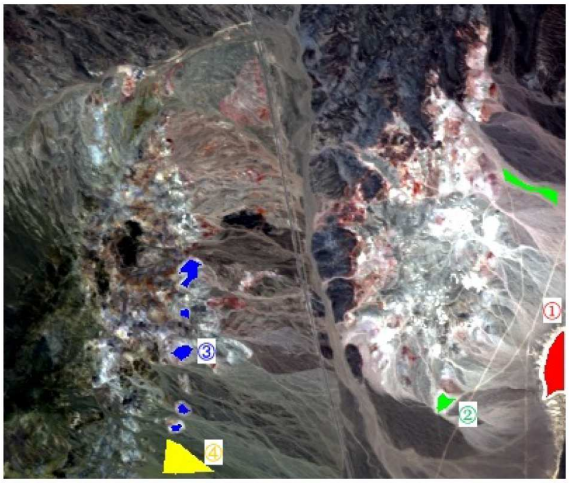

Fig. 2. True color composition of AVIRIS image and the ROIs corresponding to Na-Montmorillonite (red block), Kaolinite (green blocks), K-Alunite (blue blocks), and Muscovite (yellow block) respectively.

Figure 3 implies that the super-resolution method might be more sensitive to the low SNR originating from the atmospheric absorption or sensor performance, comparing with FLAASH. This will be further discussed in Section 4.

3.2 Comparing with Hyperion reflectance

The spaceborne Hyperion [24] image was acquired on Sep. 19, 2011 over Cuprite as well. The L1R data product was spatially resized and radiometrically scaled to a radiance image of 196 bands covering 427 nm - 2396 nm without overlap band. The spectral resolution is about 11 nm and spatial resolution about 30 m.

The reflectance image was retrieved using FLAASH with geometric parameters set according to the acquisition status and atmospheric parameters set almost the same as in Table 1 except using the 820 nm feature for water vapor retrieval. It covers an area similar to Fig. 2 and similar ROIs were drawn for averaging reflectance to suppress the influence of different spatial resolutions and geometric distortions.

To assess the performance of the super-resolution method in cross-validation between the Hyperion and the AVIRIS reflectance data, a few kinds of ROI average reflectance spectra were calculated from the AVIRIS reflectance data set mentioned in the previous subsection. These AVIRIS-derived reflectance spectra include 1) linear and 2) spline interpolations of AVIRIS FLAASH reflectance to the band positions of Hyperion, 3) convolution of AVIRIS FLAASH reflectance with the Hyperion SRFs, and 4) convolution of AVIRIS super-resolution reflectance with the Hyperion SRFs.

Figure 5 shows some of them in the spectral region 2100 nm - 2300 nm where the minerals keep absorption features and SNR are relatively high for both sensors. It could be seen that the AVIRIS-derived reflectance spectra are close to each other while differ from the Hyperion reflectance spectrum to some extent.

The possible reasons for this difference in reflectance shape include the differences between the corresponding ROI average ground objects originating from the acquisition time difference of fourteen years as well as between the SRFs, SNRs, radiometric correction uncertainties of the two sensors. However, it could not be ascertained how much each of the above differences is, because of the lack of corresponding field reference data.

Optics EXPRESS

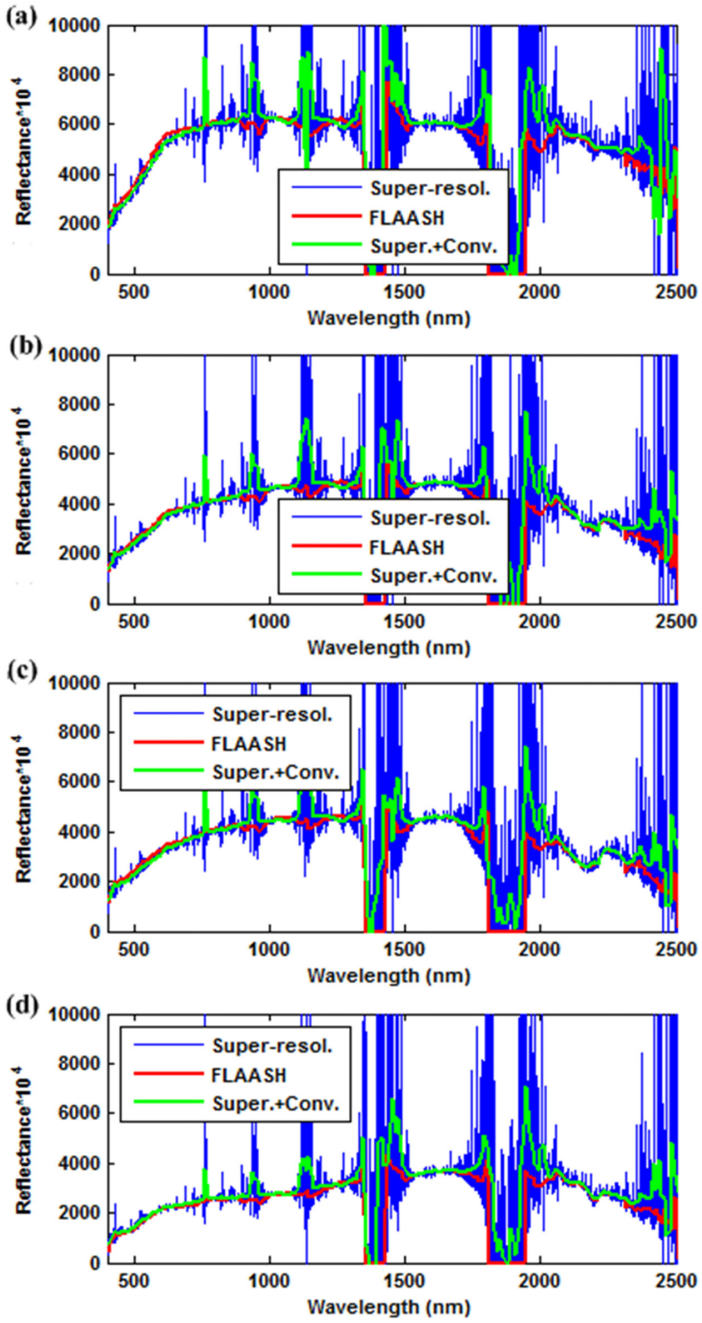

Fig. 3. The ROI average reflectance spectra of (a) Na-Montmorillonite, (b) Kaolinite, (c) K-Alunite, and (d) Muscovite from AVIRIS FLAASH reflectance, super-resolution reflectance, and convolution result of the super-resolution reflectance.

Optics EXPRESS

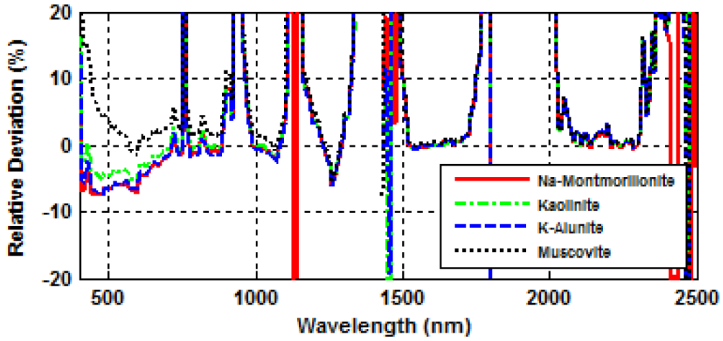

Fig. 4. Relative deviation of the convolved spectra with reference to the AVIRIS FLAASH spectra.

To examine the quantitative similarity or deviation of these AVIRIS-derived reflectance spectra with reference to the Hyperion FLAASH reflectance, the values of spectral similarity scale (SSS) [25]:

$$SSS = \sqrt{\frac{1}{N}\sum_{k=1}^{N}(x_k - y_k)^2 + (1-(\frac{1}{N-1}\sum_{k=1}^{N}\frac{(x_k-\bar{x})(y_k-\bar{y})}{\sigma_x\sigma_y})^2)^2}, \quad (8)$$

and spectral information divergence (SID) [26]:

$$SID = \sum_{k=1}^{N} p_k \log(p_k / q_k) + \sum_{k=1}^{N} q_k \log(q_k / p_k), \quad (9)$$

were calculated in the spectral region 2100 nm - 2300 nm, where N is the band number of the Hyperion FLAASH reflectance $\mathbf{y}$ and the AVIRIS result $\mathbf{x}$ to be compared, $\bar{x}$ and $\bar{y}$ the average of the elements of $\mathbf{x}$ and $\mathbf{y}$ respectively, σ_x and σ_y the standard deviation of the elements of $\mathbf{x}$ and $\mathbf{y}$ respectively, $p_k = x_k / \sum_{k=1}^{N} x_k$ and $q_k = y_k / \sum_{k=1}^{N} y_k$ the probability of each element of $\mathbf{x}$ and $\mathbf{y}$ respectively, as shown in Fig. 6. It is valid for both SSS and SID that the smaller the value is, the more similar the two spectra are.

There are decreases in both SSS and SID for ROIs of Kaolinite and K-Alunite related to the super-resolution plus convolution method compared with the other methods. For ROI of Muscovite, the SID values from all the methods are similar while the SSS value from the proposed method is a bit larger than the others. The case for ROI of Na-Montmorillonite is an exception in which the proposed method generates higher SSS and SID. It cannot be confirmed so far whether there is an obvious change of ground objects in this ROI because of the lack of corresponding data.

Generally, the spectral super-resolution plays a positive role in the comparison of data from AVIRIS and Hyperion, because it suppresses the effect of SRFs difference between the two sensors.

Optics EXPRESS

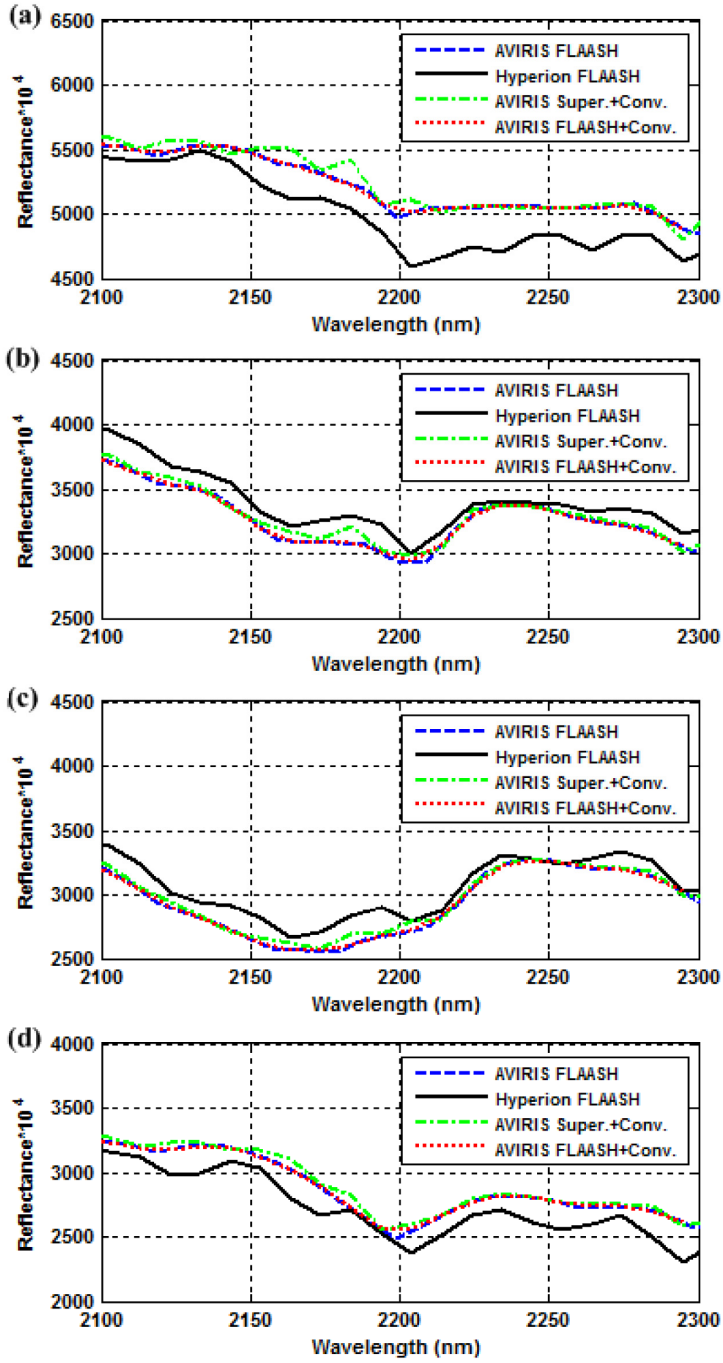

Fig. 5. Comparison of ROI average reflectance spectra of (a) Na-Montmorillonite, (b) Kaolinite, (c) K-Alunite, and (d) Muscovite for Hyperion FLAASH reflectance, AVIRIS FLAASH reflectance, Hyperion-SRF-convolved AVIRIS super-resolution reflectance, and Hyperion-SRF-convolved AVIRIS FLAASH reflectance.

Optics EXPRESS

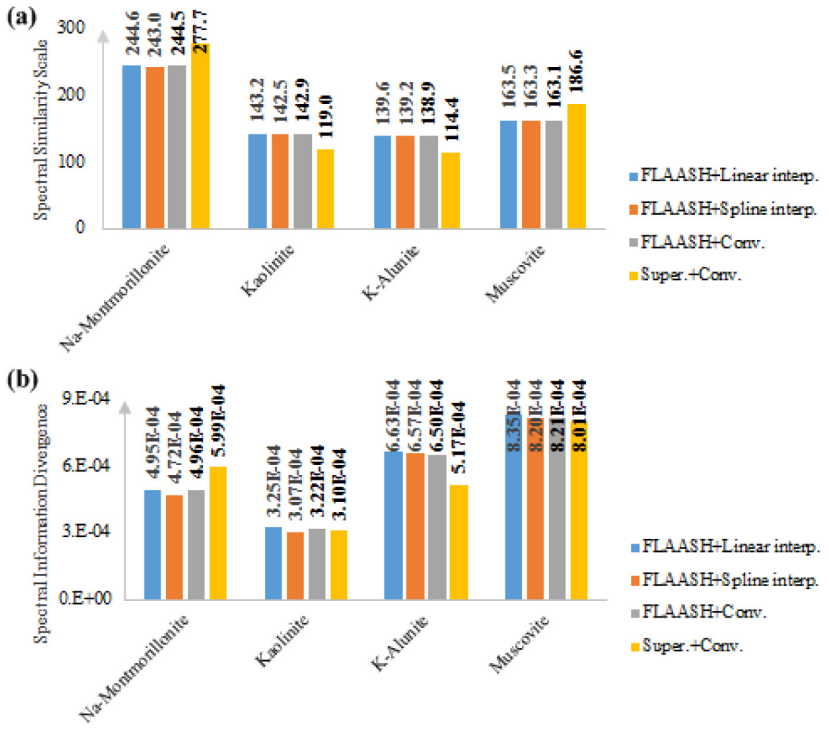

Fig. 6. (a) SSS and (b) SID values for AVIRIS results relative to Hyperion FLAASH reflectance.

4. Discussion

4.1 Sensitivity to SNR

Figure 3 implies the sensitivity of super-resolution reflectance retrieval to the SNR of the data. The spectral regions where there are large spikes in the super-resolution reflectance are around 940 nm, 1130 nm, 1400 nm, 1900 nm, and beyond 2300 nm. They correspond to an AVIRIS SNR lower than 200 with reference to the radiance passing the mid-latitude standard atmosphere from a 0.5 reflectance target at sea level illuminated at 23.5° [22]. Note that this does not imply that the super-resolution reflectance retrieval method cannot get acceptable results from radiance data with SNRs lower than 200. It is only the specific value in this case using 1997 AVIRIS data that keeps a peak SNR of 1100.

This sensitivity is also revealed by single-pixel reflectance comparison, as shown in Fig. 7. It could be seen that the Hyperion super-resolution reflectance has a similar pattern of fluctuation to AVIRIS super-resolution reflectance. The spikes get large in the spectral regions mentioned in the previous paragraph. These regions correspond to a Hyperion SNR less than 30 in pre-launch calibration with reference to 0.3 uniform albedo and 60° solar zenith angle [24].

Note that the absolute SNR values are not comparable between AVIRIS and Hyperion, because the baseline conditions for SNR calculation are different and not fully disclosed, and Hyperion might even suffer SNR deterioration after more than 10 years on orbit since launch on November 21, 2000.

Optics EXPRESS

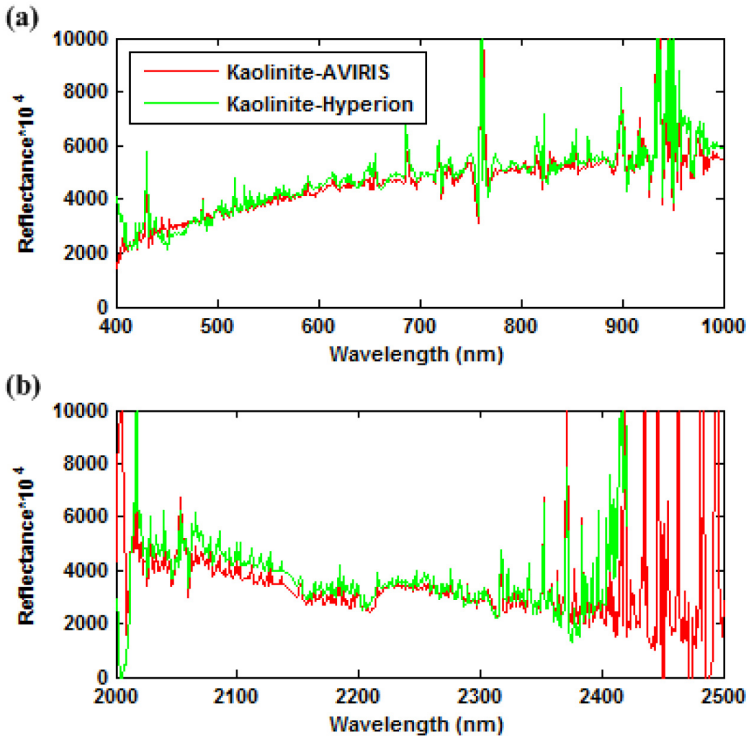

Fig. 7. The super-resolution reflectance of Kaolinite pixel from AVIRIS and Hyperion data, shown in spectral regions of (a) 400 nm - 1000 nm and (b) 2000 nm - 2500 nm.

However, both the AVIRIS and Hyperion reflectances imply that one should pay attention to the SNR of the data used in the super-resolution reflectance retrieval method. The super-resolution reflectance is not reliable in those spectral regions corresponding to relatively low SNRs because of strong atmospheric absorption and hence low incident radiation to the sensor.

4.2 High-frequency spikes in high-SNR bands

The small spikes in the spectral regions with relatively high SNRs arise from two aspects.

On one hand, although the spectral resolution of the super-resolved radiance is nominally infinity, the super-resolution processing does not gain information originally not present in the observed radiance data. Therefore, fine spectral features corresponding to high frequency that was lost during the sensor's bandpass sampling process cannot be restored any more. In other words, the super-resolution radiance is an estimate of the actual at-sensor radiance with bias, carrying much less high frequency information. This effect exists for the whole spectral range on which the radiance super-resolution is carried out. It is shown in Fig. 1 for the region around the 940 nm water vapor absorption feature.

To show it for the high-SNR spectral regions, the same MODTRAN4-based simulation data set as that is involved in Fig. 1 was used. The real at-sensor radiance spectrum was generated through MODTRAN calculation based on the settings listed in Table 2. It was convolved with the SRFs of Hyperion. Then the simulated Hyperion spectrum was spectrally super-resolved. These spectra are plotted in Fig. 8 with the relative deviation of the super-resolution radiance from the real one, taking the spectral region 2100 nm – 2300 nm as an

Optics EXPRESS

example. It shows that the high-frequency components in the real spectrum are not fully recovered in the super-resolution spectrum.

Table 2. Settings in the MODTRAN calculation.

Parameter	Value
Ground	Lambertian
Reflectance	0.3
Atmospheric Model	Mid-latitude Summer
Aerosol Model	Rural
Visibility (km)	23
Boundary Temperature (K)	293.15
CO_2 Mixing Ratio (ppmv)	390
Clouds	No
Rains	No
Filter SSI (nm)	1
Filter FWHM (nm)	1
Filter shape	Rectangle

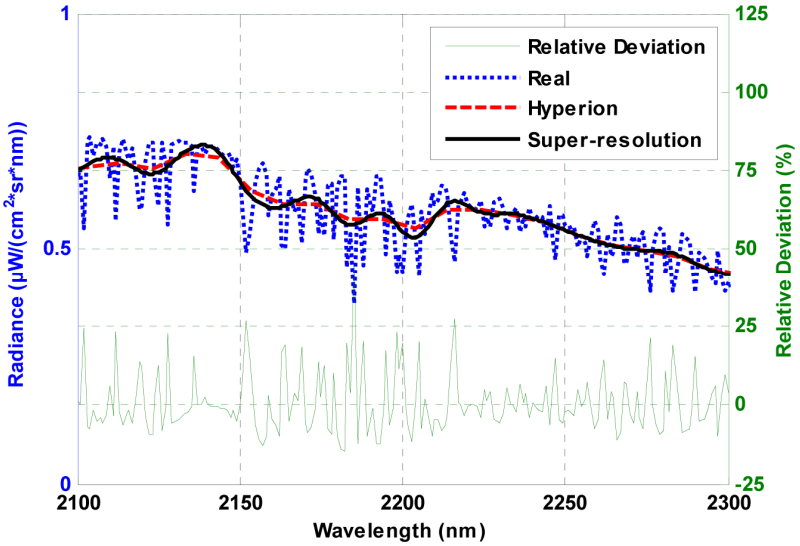

Fig. 8. The real, Hyperion, and super-resolution radiance spectra, with the relative deviation of the super-resolution spectrum, in the spectral range 2100 nm – 2300nm.

On the other hand, the high-frequency components in the super-resolution illuminative and atmospheric coefficients are fully inherited from MODTRAN calculation, which is more abundant than that in the super-resolution radiance.

Resulting from the above super-resolution radiance and coefficients, the super-resolution reflectance receives an error in the high-frequency components. The error renders itself as the spikes superimposed on reflectance curves as shown in Fig. 3.

Less spiky reflectances can be generated using traditional atmospheric correction codes with a low-pass filtered super-resolution radiance as input. However, the spectral resolution of the resulting reflectance is hence lower, which is deviating from the super-resolution purpose of this paper.

4.3 Spikes in atmospheric strong absorption bands

As shown in Fig. 3, the reflectance spikes in spectral regions around 760 nm, 940 nm, and 1100 nm - 1150 nm are obvious. The reasons are threefold.

Optics EXPRESS

The first is the restored radiance error in these regions. Figure 9 shows that step edges of spectral features such as that at 760 nm cannot be restored well enough in the super-resolution radiance spectrum. The super-resolution processing induces flattening, i.e. decreasing in slope of the edge, and overshoot, i.e. the two higher shoulders, effects around the oxygen absorption feature. These effects change the shape of radiance spectra in the atmospheric feature regions to some extent and hence contribute to the spikes in the final reflectance spectra.

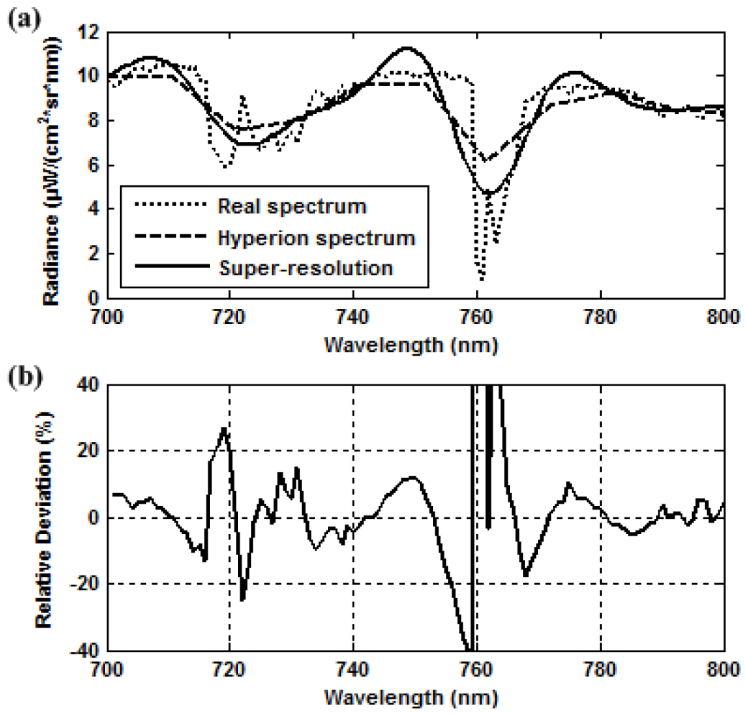

Fig. 9. The flattening and overshoot effects around steep feature of O_2 in the super-resolution radiance. (a) Adopted from [15]. Taking MODTRAN4-simulated 1-nm spectral resolution top of atmosphere radiance as the real spectrum, simulated Hyperion spectrum was generated by convolution of it, and super-resolution spectrum was retrieved from the simulated Hyperion spectrum. (b) Relative deviation of the super-resolution spectrum with reference to the real spectrum.

The second is the error of atmospheric status, especially the retrieved column water vapor, used in MODTRAN calculation for the reflectance retrieval. Since the retrieval of atmospheric status are based on the original-resolution radiance data using commonly used methods, this kind of error is at a similar level to the popular atmospheric correction methods. Its impact on the super-resolution reflectance is under-correction or over-correction in the atmospheric strong absorption bands, which is also similar to that on the results of popular atmospheric correction methods.

The third source, only for pushbroom hyperspectral sensors such as Hyperion, is the spectral calibration error including spectral shifts relative to the nominal center wavelengths and smile, also called spectral curvature, across the field of view [27]. Correction of the spectral shift and smile might lead to improvements in the absorption regions of reflectance, but is out of the scope of this paper.

Optics EXPRESS

5. Conclusions

Combining the spectral super-resolution of hyperspectral radiance data with a super-resolution improvement of FLAASH atmospheric correction method, super-resolution reflectance could be retrieved from remotely sensed images for bands with enough SNR, i.e. high incident radiation and sensor responsivity.

By bandpass sampling of the super-resolution reflectance, reflectance of any spectral sampling characteristic could be generated. The method was validated using AVIRIS and Hyperion data.

When super-resolution reflectance was convolved with the SRFs of the same sensor, as for AVIRIS in this paper, the generated reflectance was found to be almost identical to the direct FLAASH result except for the bands around atmospheric absorption features and with low SNR.

When super-resolution reflectance was convolved with SRFs of another sensor, e.g. from AVIRIS to Hyperion, which have similar spectral resolution, the generated reflectance was superior to those generated by the commonly-used interpolation or convolution methods in the sense of suppressing the effect of SRFs difference.

For the same reason, the super-resolution reflectance would also play a positive role in cross-validation of data from two sensors with larger differences in spectral resolution.

The high-frequency spikes in high-SNR bands of the super-resolution reflectance come from mismatch of the high-frequency components between the super-resolution radiance and the illumination and atmospheric coefficients. An improvement about high-frequency compensation to the super-resolution radiance based on MODTRAN calculations is to be considered in the near future.

Funding

China Scholarship Council (CSC) (201406025107); National Natural Science Foundation of China (NSFC) (41201324).

Acknowledgments

The AVIRIS image was obtained from the Jet Propulsion Laboratory and the Hyperion image from the US Geological Survey. The authors would thank the anonymous reviewer for the constructive and detailed comments.